Supplementary information

Nano-confined controllable crystallization in supramolecular polymeric membranes for ultra-selective desalination

Gang Lu[1]*, Hubao A[2], Yuanyuan Zhao[3], Yan Zhao[4], Hengyue Xu[5], Wentao Shang[6], Xi Chen[1], Jiawei Sun[1], Huacheng Zhang[7], Jun Wu[8], Bing Dai[9], Bart Van der Bruggen[4], Raf Dewil[4,10], Alicia Kyoungjin An[1,11]*, Shuang Zheng[12,13]*

[1]School of Energy and Environment, City University of Hong Kong, Hong Kong 999077, China

[2]State Key Laboratory of Water Resources and Hydropower Engineering Science, Wuhan University, Wuhan 430072, China

[3]School of Fashion and Textiles, The Hong Kong Polytechnic University, Hong Kong 999077, China

[4]Department of Chemical Engineering, KU Leuven, Leuven, Belgium

[5]Department of Chemistry, Tsinghua University, Beijing 10084, China

[6]Energy and Electricity Research Center, International Energy College, Jinan University, Guangdong 519070, China

[7]Chemical and Environmental Engineering, School of Engineering, RMIT University, Melbourne, VIC, 3000, Australia

[8]Yantai Research Institute, Harbin Engineering University, Yantai, Shandong 264006, China

[9]Guangdong Laboratory of Artificial Intelligence and Digital Economy (SZ), School of Biomedical Engineering, Shenzhen University, Shenzhen 518060, P. R. China

[10]Department of Engineering Science, University of Oxford, Oxford OX1 3PJ, United Kingdom.

[11]Department of Chemical and Biological Engineering, The Hong Kong University of Science and Technology, Hong Kong 999077, China

[12]Department of Civil Engineering, The University of Hong Kong, Hong Kong, China

[13]Kavli Institute for Nanoscience Discovery, Department of Physiology, Anatomy, & Genetics, University of Oxford, Oxford, OX1 3QU, UK

Corresponding Authors: G. Lu, E-mail: ganglu2-c@my.cityu.edu.hk

A. K. An, Email: alicia.kjan@ust.hk

S. Zheng, Email: shuang.zheng@dpag.ox.ac.uk

Supplementary Figures

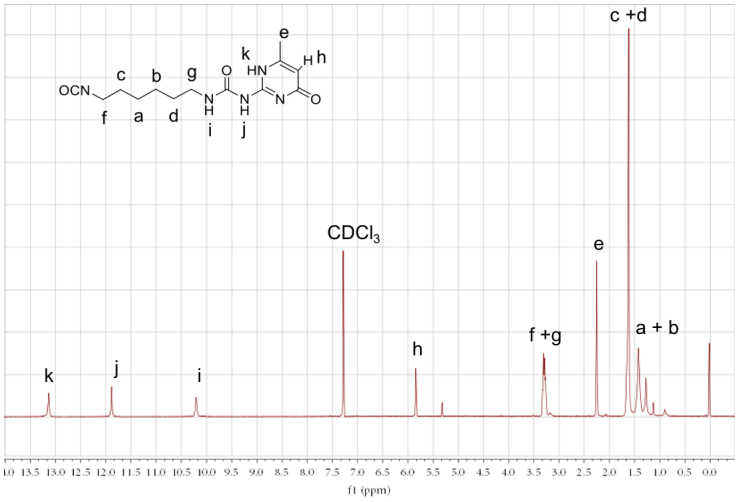

Figure S1. ^{1}H NMR spectrum of UPy-NCO motif in chloroform-d.

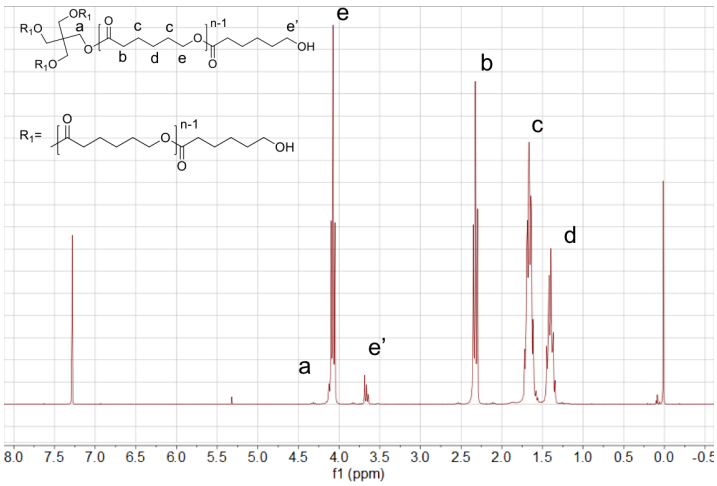

Figure S2. ^{1}H NMR spectrum of tetra-PCL-OH in chloroform-d.

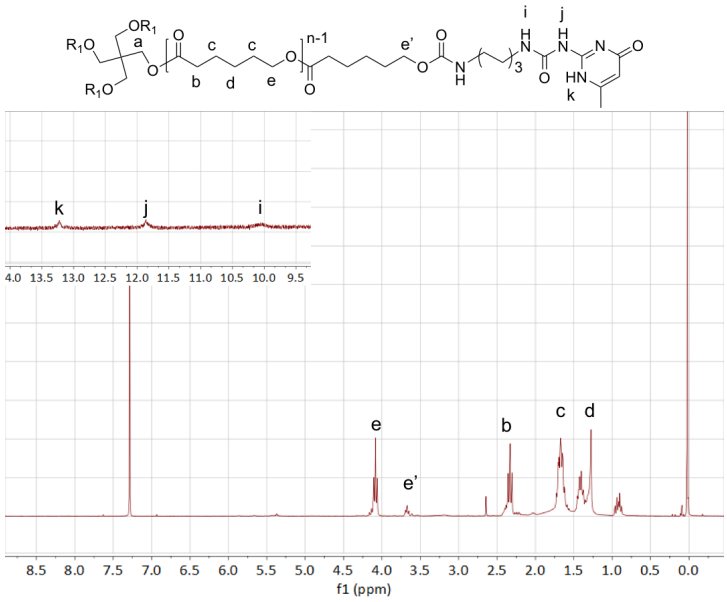

Figure S3. ^{1}H NMR spectrum of tetra-PCL-UPy in chloroform-d.

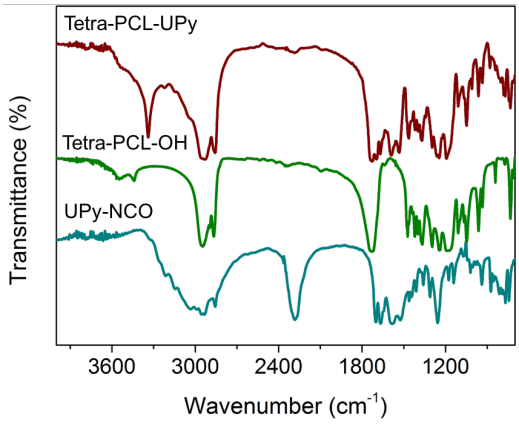

Figure S4. FTIR spectra of UPy-NCO, Tetra-PCL-OH, and Tetra-PCL-UPy.

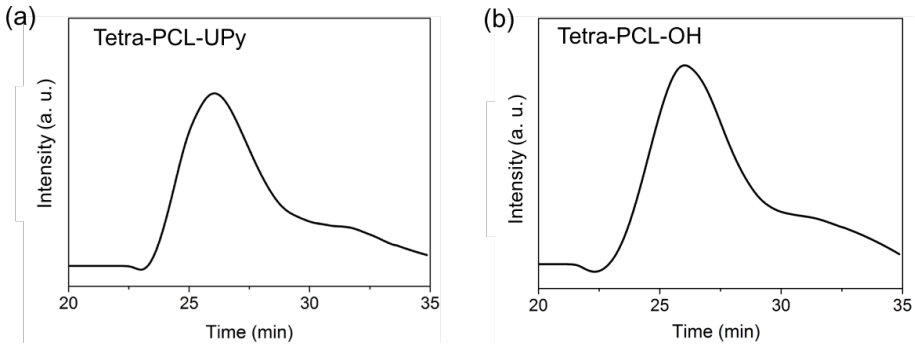

Figure S5. GPC profile of tetra-PCL-UPy (a) and Tetra-PCL-OH (b).

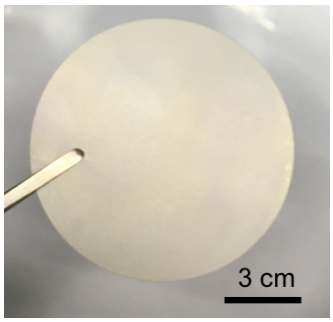

Figure S6. Optical image of the NCC-6 membrane.

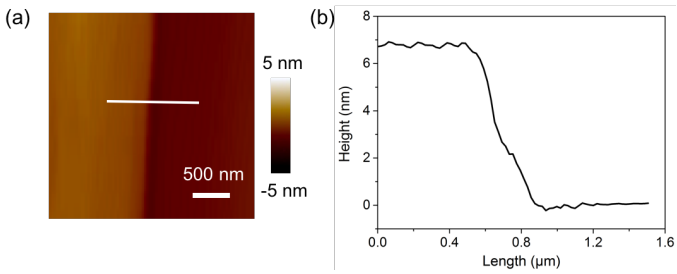

Figure S7. The thickness image (a) and profile (b) of NRC membrane determined by AFM. The membrane was prepared by spreading a 2 mg/mL solution of Tetra-PCL-OH on the water surface. The resulting nanofilm was then transferred and deposited onto a silicon wafer for AFM analysis. The measured thickness of the membrane was approximately 6.4 ± 0.3 nm.

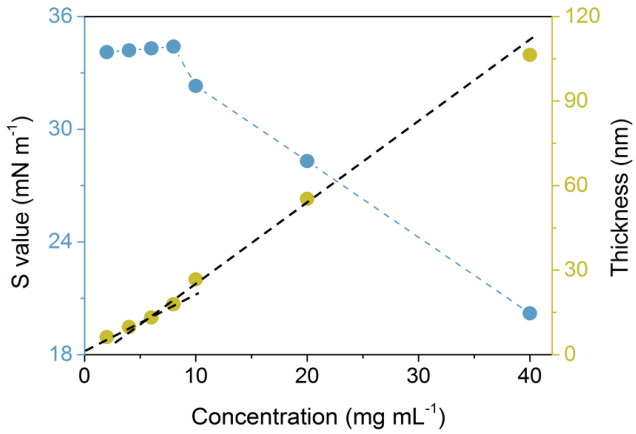

Figure S8. Variation of S value and thickness of NCC membranes with concentrations.

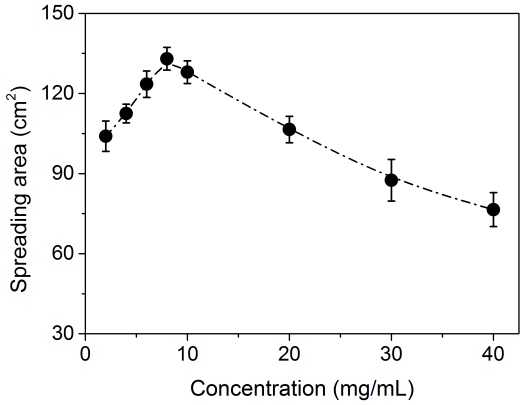

Figure S9. Variation between spreading area of NCC membrane and solution concentrations. Error bars represent the standard deviation from three duplicate experiments.

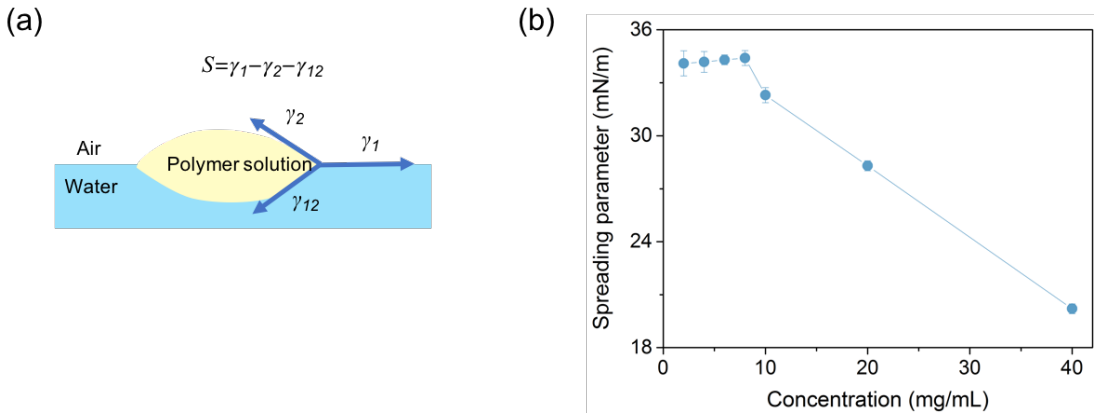

Figure S10. (a) Surface tension parameters were shown when the microdroplet was deposited on water interface. (b) Spreading parameter changed with different concentrations of tetra-PCL-UPy. Error bars represent the standard deviation from three duplicate experiments.

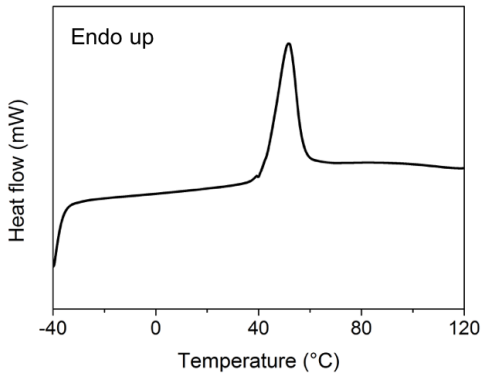

Figure S11. DSC curve of the NCC-6 membrane.

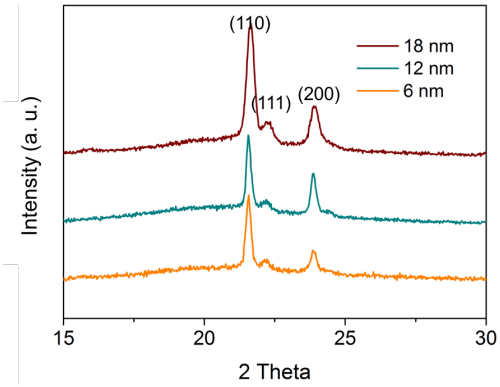

Figure S12. GIXRD patterns of NCC membranes with different thickness.

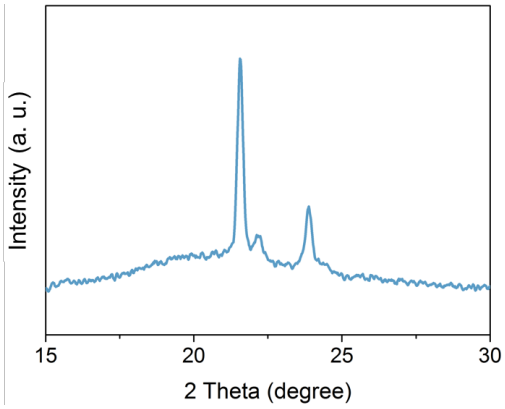

Figure S13. GIXRD pattern of the 6 nm NRC-6 membrane.

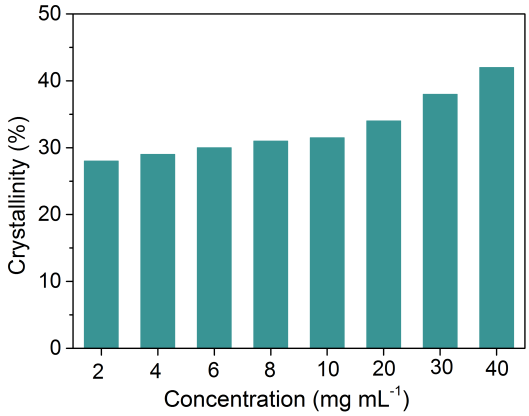

Figure S14. The crystallinity of NCC membranes with different concentrations.

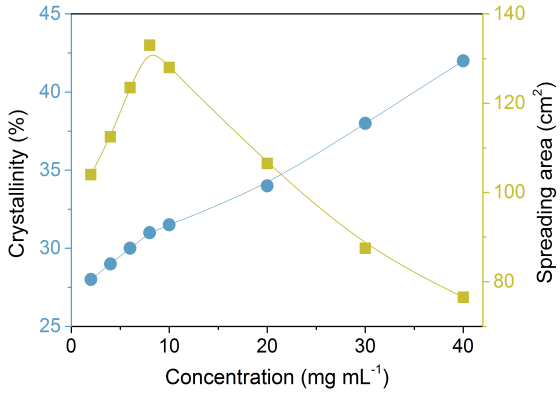

Figure S15. The crystallinity and spreading area of NCC membranes with concentrations.

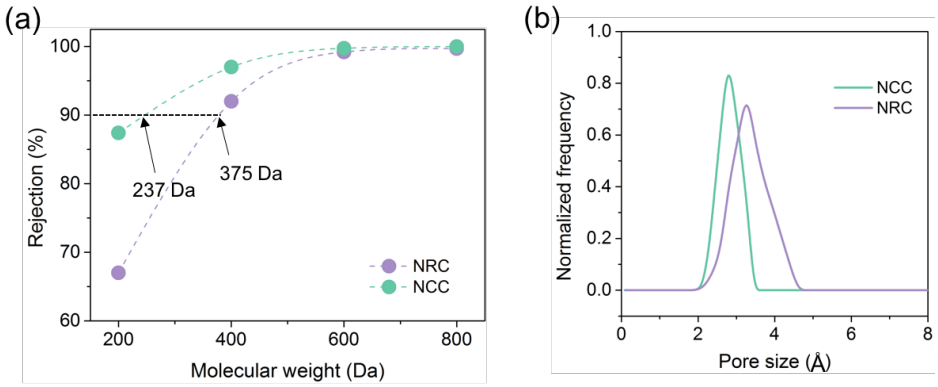

Figure S16. (a) Rejection of neutral PEG solutes through the NCC-6 and the NRC-6 membranes. (b) Experimental pore size of the NCC-6 and NRC-6 membranes.

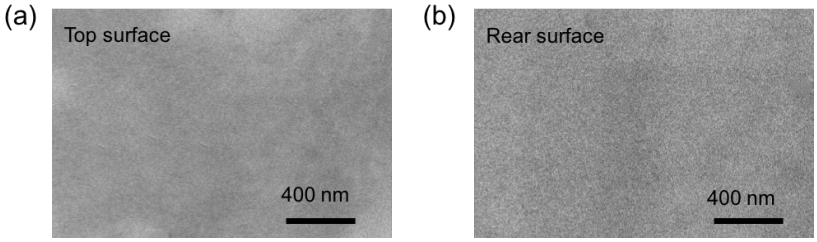

Figure S17. SEM images of top (a) and rear (b) surface of the NCC-6 membrane.

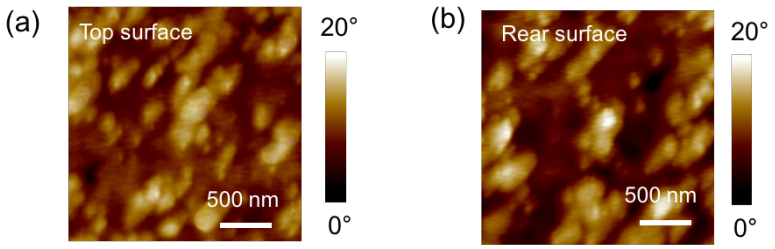

Figure S18. AFM images of top (a) and rear (b) surface of the NRC-6 membrane.

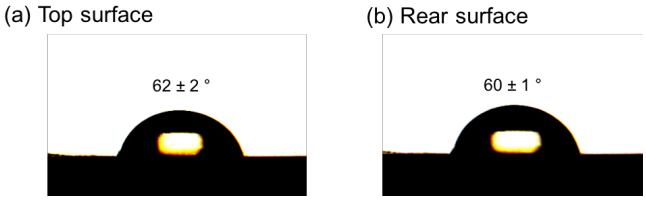

Figure S19. Water contact angle of top (a) and rear (b) surface of NRC-6 membrane.

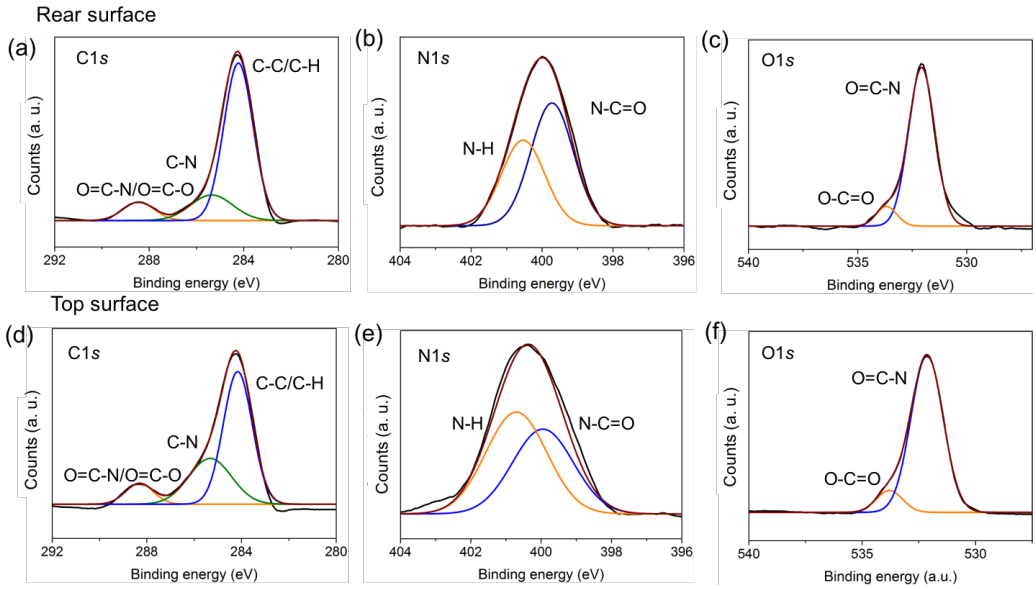

Figure S20. High resolution XPS spectra of rear surface (a-c) and top surface (d-f) of the NCC membrane.

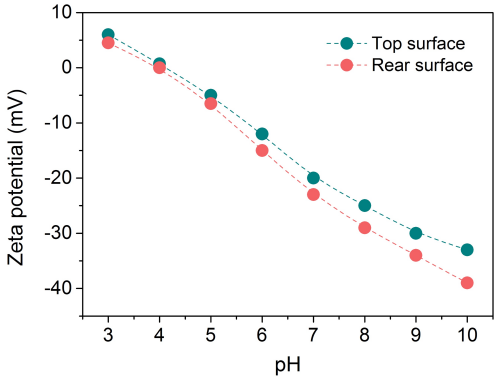

Figure S21. Surface zeta potential of two sides of the NCC-6 membrane.

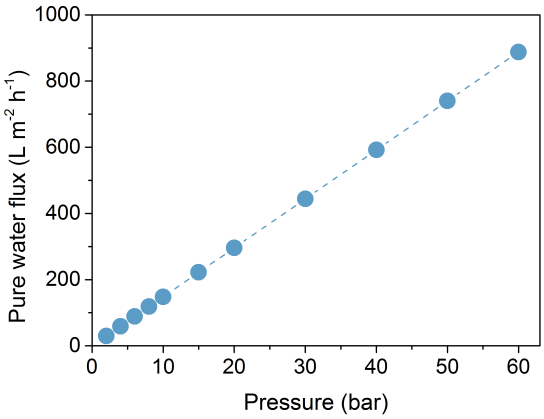

Figure S22. Variation between pure water flux and pressure through NCC-6 membrane

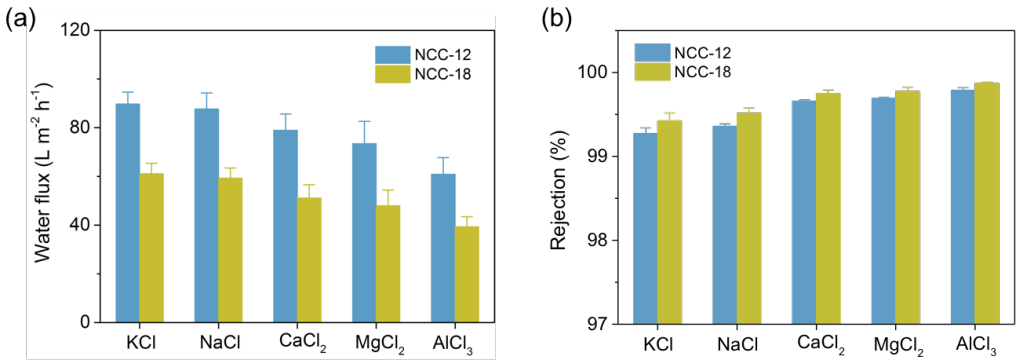

Figure S23. Water flux (a) and single salt rejection (b) of the NCC-12 and NRC-18 membranes. The experimental conditions are as follows: an effective membrane area of 3 cm^2, a 1000 ppm salt feed solution, a crossflow velocity of 50 L h^{-1}, and a constant pressure of 10 bar. Error bars represent the standard deviation from three duplicate experiments.

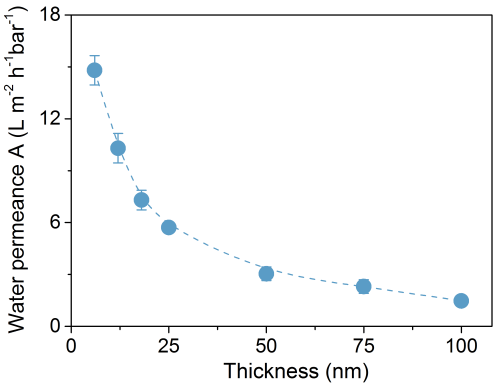

Figure S24. Variation between water permeance and thickness of NCC membranes at 10 bar. Error bars represent the standard deviation from three duplicate experiments.

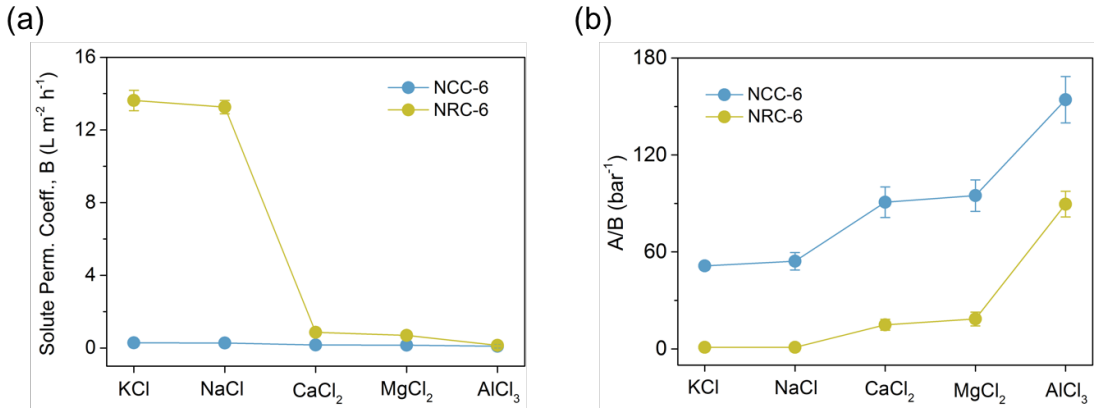

Figure S25. Solute permeability coefficient (a) and water-solute selectivity (b) of NCC-6 and NRC-6 membranes. Error bars represent the standard deviation from three duplicate experiments.

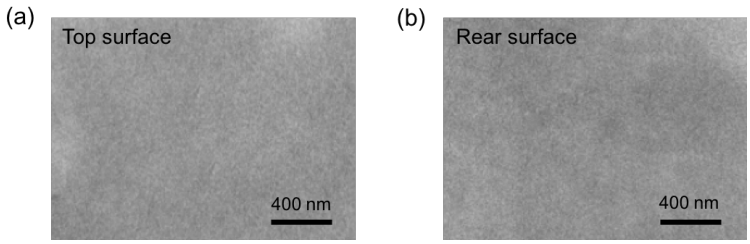

Figure S26. SEM surface characterization on top surface (a) and rear surface (b) of NCC-6 membrane after 7-day separation.

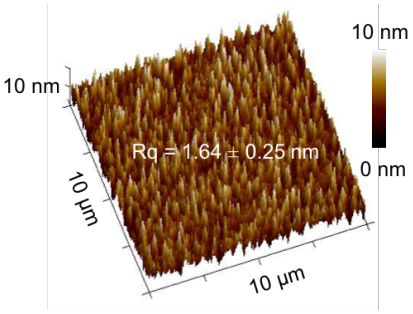

Figure S27. The roughness of NCC-6 membrane determined by AFM after 7-day separation.

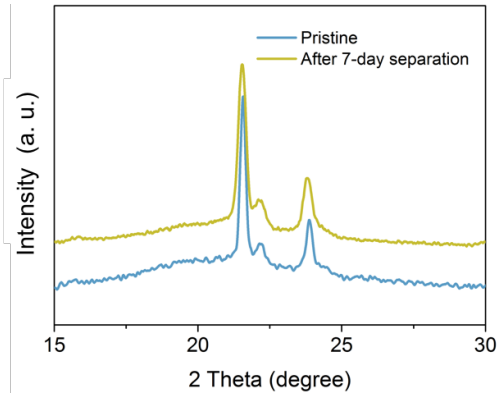

Figure S28. XRD profile of NCC-6 membrane determined by XRD after 7-day separation.

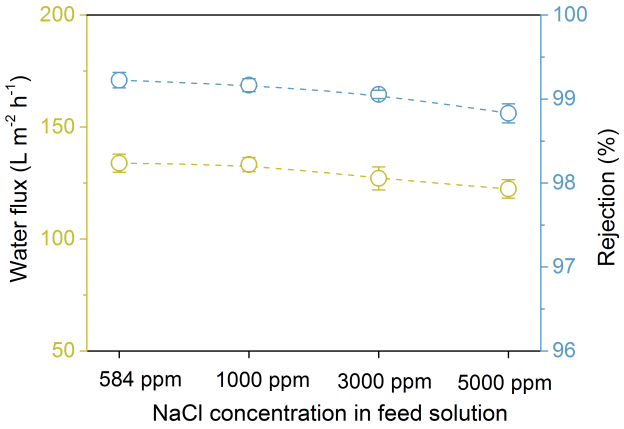

Figure S29. RO separation performance of different concentrations of NaCl solution treated by 10 bar applied pressure. Error bars represent the standard deviation from three duplicate experiments.

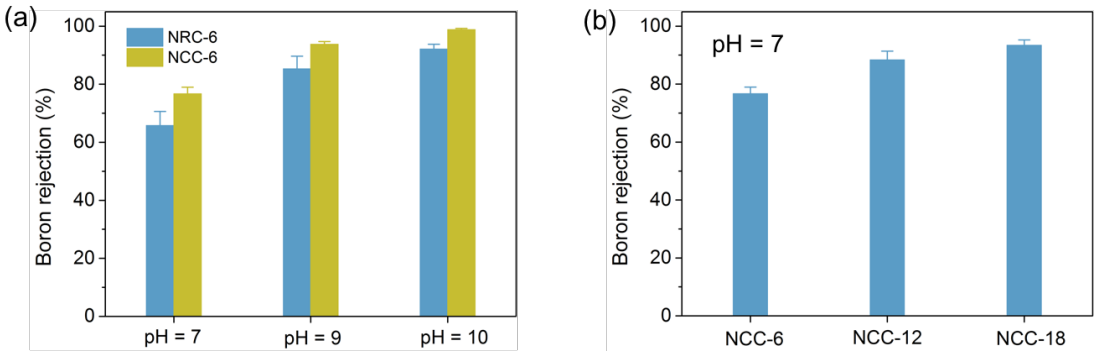

Figure S30. (a) Boron rejection of different pH solution treated by the NRC-6 and NCC-6 membranes. (b) Boron rejection of pH = 7 solution treated by the NCC membranes. The feed solution concentration of boric acid $B(OH)_3$ was 5 ppm, and NaOH was used to regulate pH. Error bars represent the standard deviation from three duplicate experiments.

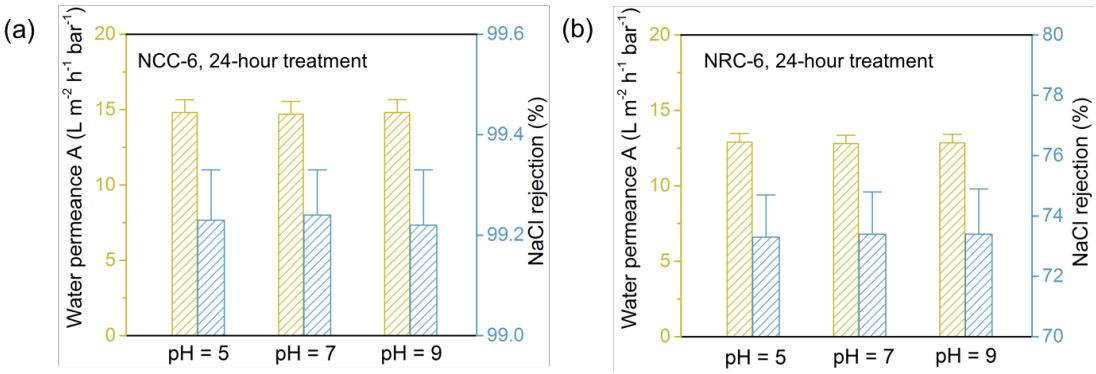

Figure S31. The water permeance (a) and NaCl rejection (b) of the NCC-6 and the NRC-6 membranes that were soaked in 200 ppm NaClO solution at different pH for 24-h. The pH values of NaClO solution were regulated to 5, 7, and 9, using hydrogen chloride and sodium hydroxide solutions. The container was completely wrapped with tin foil and stored in the dark. Error bars represent the standard deviation from three duplicate experiments.

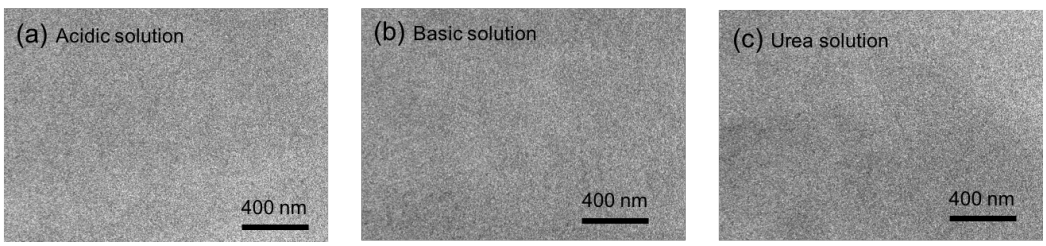

Figure S32. SEM images of NCC-6 membranes that were treated with acidic (pH = 3) (a), basic (pH = 11) (b), and urea (1 wt%) (c) solutions for 24 hours.

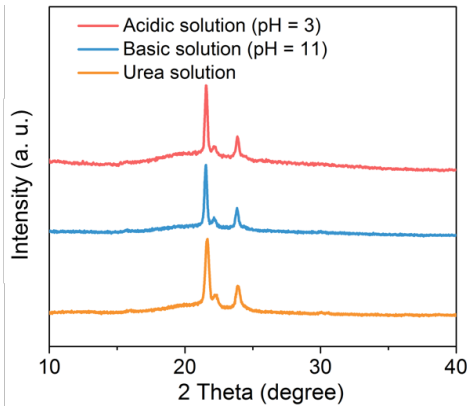

Figure S33. XRD profiles of NCC-6 membranes that was treated with acidic (pH = 3), basic (pH = 11), and urea (1 wt%) solutions for 24 hours.

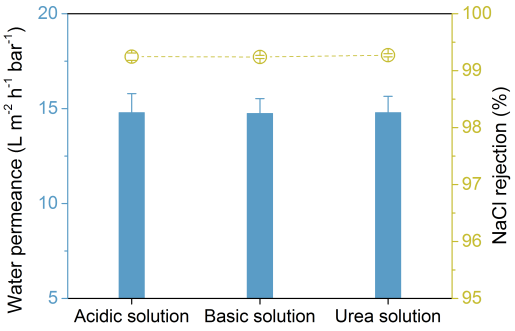

Figure S34. The water permeance and NaCl rejection of NCC-6 membranes that was treated with acidic (pH = 3), basic (pH = 11), and urea (1 wt%) solutions for 24 hours. Error bars represent the standard deviation from three duplicate experiments.

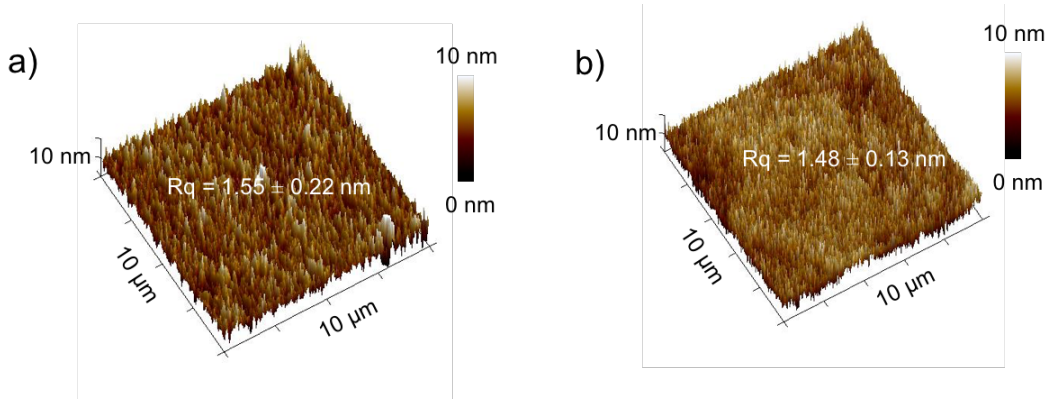

Figure S35. Roughness measurements of NCC-6 membranes that were soaked in water (a) and 1 M NaCl solution (b). In comparison to the pristine value, the Rq value witness no obvious changes when treated in two conditions, showing good stability.

Simulation method

Molecular models of tetra-PCL-OH and tetra-PCL-UPy

The two tetra-oligomers with distinct end-functional groups in this work are tetra-PCL-OH and tetra-PCL-UPy, respectively, whose initial structures are shown in Fig. S36a-b drawn by ChemDraw. The interactions between atoms in above structures are described by GROMOCS 54A7 force field,[1] and force field parameters are further corrected via the Automated force field Topology Builder (ATB).[2] The equilibrium configurations of tetra-PCL-OH and tetra-PCL-UPy produced by ATB are shown in Fig. S36c-d, which are used for subsequent simulations, including density calculation, voids analysis, tetra-oligomer/water molecule interactions identification (i.e., interfacial energy and hydrogen bonding). Considering the computational efficiency and accuracy, a classical water molecule model SPC/E is adopted here.

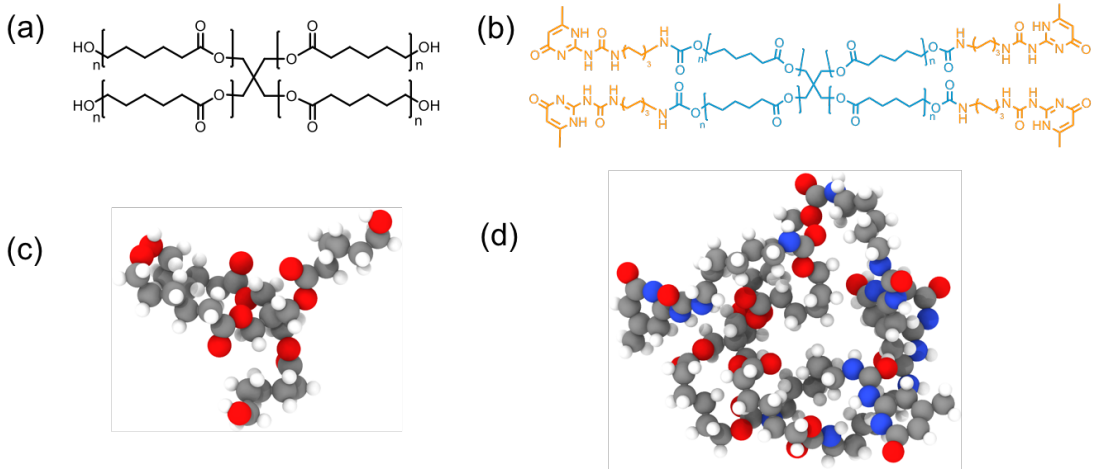

Figure S36. The molecular structure of tetra-PCL-OH (a) and tetra-PCL-UPy (b), respectively. The equilibrium configurations of tetra-PCL-OH (c) and tetra-PCL-UPy (d) produced by ATB, respectively. In the c and d, grey, red, white and blue balls represent the carbon, oxygen, hydrogen and nitrogen atoms, respectively.

Tetra-oligomer/water molecule interactions identification

To identify the interactions between Tetra-oligomers and water molecules, we build two sandwich models as shown in Fig. S37, where tetra-oligomer layers are distributed between two layers of water molecules. Then, two sandwich models are relaxed at ambient conditions (1 atm and 300K) until reaching equilibrium state. Subsequently, another 2 ns simulations are performed to collect the configurations of models to identify the tetra-oligomer/water molecule interactions, i.e, interaction energy and hydrogen bonding interactions. To obtain interaction energy between tetra-oligomer and water molecules, we first calculate the interactions energy $U_{T\text{-}W}$ between tetra-oligomer and water molecules, calculation details are described in detail elsewhere[3]. To facilitate the comparison of the strength of the interaction between Tetra-oligomers and water molecules, we further calculate the areal density of interactions energy $E_{T\text{-}W}$ (see Eq. S1). We also obtain the H-Bonding number $N_{H\text{-}B}$ between Tetra-oligomers and water molecules, the forming conditions can be found in the reference.[4] Similarly, to facilitate the comparison of hydrogen bonding interactions between two Tetra-oligomers and water molecules, we calculate the areal density of H-Bonding number $S_{H\text{-}B}$ (see Eq. S2).

	$E_{T\text{-}W} = U_{T\text{-}W}/2A$	S1
	$S_{H\text{-}B} = N_{H\text{-}B}/2A$	S2

where A represents the area of the interface between tetra-oligomers and water molecules, and a factor of 2 is utilized because there are two interfaces in sandwich models.

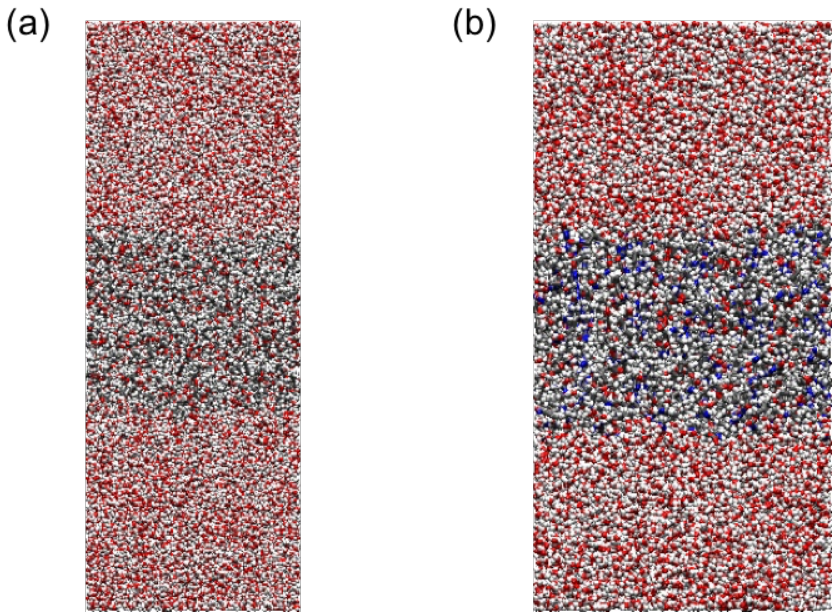

Figure S37. Simulation models for Tetra-oligomer/water molecule interactions identification. (a) The sandwich model composed of tetra-PCL-OH and water molecules; (b) The sandwich model composed of tetra-PCL-UPy and water molecules.

Density calculation and voids analysis

In order to comprehensively evaluate the density and void characteristics of tetra-PCL-OH and tetra-PCL-UPy, we consider two representative scenarios: before and after interaction with water. Such settings not only enable us to quantify the density and void characteristics of these two kinds of tetra-oligomers under varying conditions but also facilitate the determination of how the properties of tetra-oligomers evolve following interaction with water.

In the scenario involving pure tetra-oligomers (excluding tetra-oligomer–water interactions), two simulation boxes are constructed, each filled with either tetra-PCL-OH (see Figure S38a, comprising 125 tetra-PCL-OH oligomers and 11,625 atoms) or tetra-PCL-UPy (see Figure S38b, comprising 48 tetra-PCL-UPy oligomers and 12,336 atoms). Subsequently, both constructed simulation boxes are relaxed at ambient conditions (1 atm and 300K) until reaching an equilibrium state. Subsequently, an additional 2 ns of simulations are conducted to gather molecular configurations within the simulation boxes for density calculation and voids analysis. For MD simulations, to mitigate statistical fluctuations and ensure result validity, we conducted an additional 2 ns of simulations after reaching equilibrium. Molecular configurations within the simulation boxes were gathered every 100 ps for density calculations and void analysis. Each simulation was repeated independently three times, and the averaged values from these

trials were used to obtain robust and reliable data, ensuring the precision and statistical stability of the results.

The density of tetra-oligomers is determined by dividing the sum of the masses of all atoms in the simulated box by the volume of the simulated box. Voids analysis is performed using PoreBlazer,[5] during which the size of probe is fixed to 1.0 Å. In this work, we analysis tow critical voids characteristics, i.e., fractional free volume and pore size distributions.

To quantify the density and void characteristics of two kinds of tetra-oligomers after interaction with water, we initiate simulations of tetra-oligomer/water interactions following the method and procedures as outlined in the preceding section. Once the tetra-oligomer/water simulation system reaches an equilibrium state, we extract the structures of tetra-oligomers for subsequent density calculation and voids analysis. The analytical method employed is consistent with that utilized in the scenario involving pure tetra-oligomers.

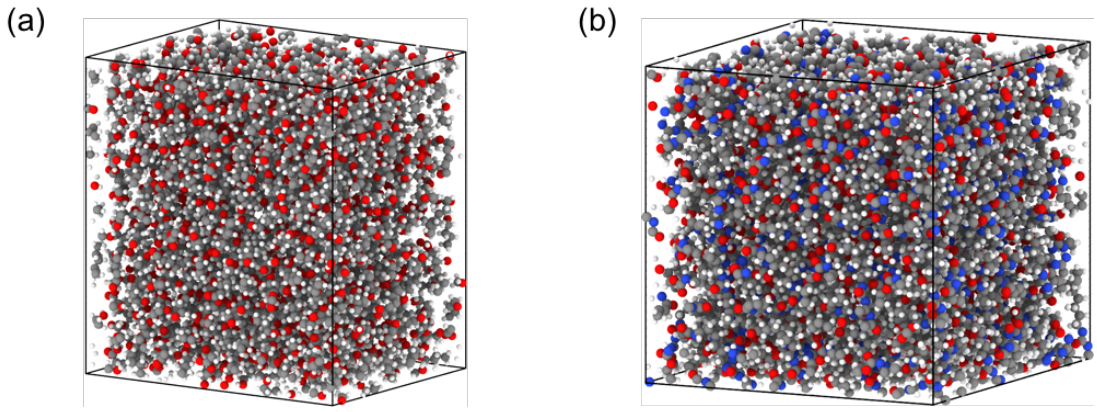

Figure S38. Simulation models for density calculation and voids analysis. (a) simulation boxes filled with tetra-PCL-OH; (b) simulation boxes filled with tetra-PCL-UPy.

Simulations details

All MD simulations in this work are carried out in NPT ensemble (temperature = 300 K, pressure = 1 atm), both the temperature and pressure are controlled using the Nosé-Hoover method.[6] The position and velocity of atoms are updated through the velocity-Verlet algorithm with a time step of 2 fs.[7] Moreover, periodic boundary conditions are adopted in all directions. All MD simulations are performed using the classical platform LAMMPS,[8] and the resulting trajectories are visualized in the open visualization tools OVITO[9] and VMD[10].

Supplementary Tables

Table S1. Spreading coefficients under with different concentrations of tetra-PCL-UPy.

Surface tension at 20 °C (mN/m)	2 mg/mL	4 mg/mL	6 mg/mL	8 mg/mL	10 mg/mL	20 mg/mL	40 mg/mL
S	34.1 ± 0.7	34.2 ± 0.6	34.3 ± 0.3	34.4 ± 0.4	32.3 ± 0.4	28.3 ± 0.3	20.2 ± 0.3

Table S2. Surface chemical components of the two sides of the NCC membrane.

Membrane	C1s			N1s			O1s		
	Energy (eV)	Species	%	Energy (eV)	Species	%	Energy (eV)	Species	%
Top surface	284.6	C-H C-C	70.1	399.7	N-C=O	60.4	532	O=C-N	87.6
	286	C-N	18.7	400.5	N-H	39.6	533.5	O=C-O	12.4
	288	O-C=O O-C=N	11.2						
Rear surface	284.6	C-H C-C	68.3	399.7	N-C=O	48.7	532	O=C-N	90.3
	286	C-N	19.5	400.5	N-H	51.3	533.5	O=C-O	9.7
	288	O-C=O O-C=N	12.2						

Figure S3. Summary of the desalination performance of the NCC-6 and NRC-6 membrane driven by the external pressure. (Feed solutions: 1000 ppm; applied pressure: 10 bar)

Feed solution (pure water or salt solution)	NCC-6					NRC-6				
	Water flux (L m^{-2} h^{-1})	Rejection (%)	A (L m^{-2} h^{-1} bar^{-1})	B (L m^{-2} h^{-1})	A/B (bar^{-1})	Water flux (L m^{-2} h^{-1})	Rejection (%)	A (L m^{-2} h^{-1} bar^{-1})	B (L m^{-2} h^{-1})	A/B (bar^{-1})
KCl	136 ± 5.3	99.18± 0.06	14.8	0.288	51.4	118 ± 5.3	72.7 ± 1.3	12.9	13.62	0.95
NaCl	133 ± 3.2	99.23 ± 0.09	14.8	0.273	54.2	115 ± 5.3	73.3 ± 1.4	12.9	13.26	0.97
$CaCl_2$	121 ± 3.8	99.55 ± 0.05	14.8	0.163	90.8	103 ± 2.3	97.7 ± 0.5	12.9	0.865	14.9
$MgCl_2$	119 ± 3.4	99.57 ± 0.06	14.8	0.156	94.87	100 ± 4.7	98.1 ± 0.28	12.9	0.699	18.5
$AlCl_3$	102 ± 3.2	99.74 ± 0.03	14.8	0.096	154.15	79 ± 4.2	99.6 ± 0.14	12.9	0.144	89.6

Figure S4. Summary of the desalination performance of the NCC-12 and NCC-18 membrane driven by the external pressure. (Feed solutions: 1000 ppm; applied pressure: 10 bar)

Feed solution (pure water or salt solution)	NCC-12					NCC-18				
	Water flux (L m^{-2} h^{-1})	Rejection (%)	A (L m^{-2} h^{-1} bar^{-1})	B (L m^{-2} h^{-1})	A/B (bar^{-1})	Water flux (L m^{-2} h^{-1})	Rejection (%)	A (L m^{-2} h^{-1} bar^{-1})	B (L m^{-2} h^{-1})	A/B (bar^{-1})
KCl	89.8 ± 4.8	99.28± 0.06	10.2	0.27	37.78	61.1 ± 4.3	99.43± 0.09	7.3	0.19	38.42
NaCl	87.7 ± 6.5	99.36 ± 0.03	10.2	0.24	42.5	59.3 ± 4.2	99.52 ± 0.06	7.3	0.16	45.63
$CaCl_2$	78.9 ± 6.6	99.66 ± 0.02	10.2	0.12	85	51.2 ± 5.4	99.75 ± 0.04	7.3	0.08	91.25
$MgCl_2$	73.6 ± 9.2	99.69 ± 0.02	10.2	0.11	95.73	48 ± 6.4	99.78 ± 0.05	7.3	0.07	104.29
$AlCl_3$	60.9 ± 6.8	99.79 ± 0.03	10.2	0.07	145.72	39.4 ± 4.1	99.87 ± 0.02	7.3	0.03	243.33

Reference

1. Schmid, N. et al. Definition and testing of the GROMOS force-field versions 54A7 and 54B7. *Eur. Biophys. J* **40**, 843-856 (2011).
2. Malde, A.K. et al. An automated force field topology builder (ATB) and repository: version 1.0. *J. Chem. Theory Comput.* **7**, 4026-4037 (2011).
3. Yang, Z., Hu, R. & Chen, Y. Molecular Origin of Wetting Characteristics on Mineral Surfaces. *Langmuir* **39**, 2932–2942 (2023).

4. Hubao, A., Yang, Z., Hu, R., Chen, Y.-F. & Yang, L. Effect of solid–liquid interactions on substrate wettability and dynamic spreading of nanodroplets: a molecular dynamics study. *J. Phys. Chem. C* **124**, 23260-23269 (2020).
5. Sarkisov, L. & Harrison, A. Computational structure characterisation tools in application to ordered and disordered porous materials. *Mol. Simul.* **37**, 1248-1257 (2011).
6. Liu, L. et al. A Superstrong and Reversible Ionic Crystal‐Based Adhesive Inspired by Ice Adhesion. *Angew. Chem.* **133**, 9030-9041 (2021).
7. Hubao, A., Yang, Z., Hu, R. & Chen, Y.-F. Roles of energy dissipation and asymmetric wettability in spontaneous imbibition dynamics in a nanochannel. *J. Colloid Interface Sci.* **607**, 1023-1035 (2022).
8. Thompson, A.P. et al. LAMMPS-a flexible simulation tool for particle-based materials modeling at the atomic, meso, and continuum scales. *Comput. Phys. Commun.* **271**, 108171 (2022).
9. Stukowski, A. Visualization and analysis of atomistic simulation data with OVITO–the Open Visualization Tool. *Model. Simul. Mater. Sci. Eng.* **18**, 015012 (2009).
10. Humphrey, W., Dalke, A. & Schulten, K. VMD: visual molecular dynamics. *J. Mol. Graph.* **14**, 33-38 (1996).